DTC visitor project

Impact assessment of cloud-affected AMSU-A radiance assimilation in TC inner-core region using hybrid data assimilation approaches

Report

Man Zhang*

July, 2014

*Current contact: Dr. Man Zhang, NOAA ESRL/GSD, and CIRES/University of Colorado-Boulder; E-mail: man.zhang@noaa.gov

1. Introduction

The new frontier for improvement in NWP models from the point of view of defining the model initial state is the full use of available satellite and ground-based data, including cloud and precipitation-affected observations. Current satellite-based observations are rich in global cloud-related information. New sensors such as the Moderate Resolution Imaging Spectroradiometer (MODIS) on board the *Terra* and *Aqua* satellites, the cloud profiling radar (CPR) on board *CALIPSO* are revealing the complex two-dimensional and three-dimensional structures of clouds. The challenge now is to extract the largest amount of information about the cloudy atmosphere from this wealth of data by using state-of-the art modeling and assimilation systems.

The assimilation of cloud observations, using global or regional numerical weather prediction (NWP) systems, has been hampered by several factors (Errico et al., 2007). To date, a large percentage of satellite observations affected by clouds and precipitation are not included in global or regional analysis systems mainly because of the difficulties in defining background error statistics for cloud control variables. As a result, cloudy areas are less constrained by observations than cloud-free areas.

In this study we attempt to demonstrate that the prototype ensemble-based data assimilation system is technically ready to assimilate cloud observations in TC core area, thanks to the inclusion of a simplified moist physics schemes. As a first step, the AMSU-A radiances are directly assimilated. It is recognized that dealing with the raw radiance measurements through the appropriate observation operators allow for both a more consistent treatment of the observations within the model framework and a full utilization of the model sensitivity to observations (Vukićević et al. 2004; Moreau et al. 2004). Thus, one of the objectives of this project is to examine the performance of the direct assimilation of AMSU-A radiances in TC core area. The next section describes the general methodology and briefly provides details about the HVEADS system. Section 4 introduces the components of inclusion of cloudy radiances, Section 4 presents the outcome of the cloudy radiance assimilation experiment with respect to a reference run. The background error covariance from the HVEDAS (i.e., MLEF-HWRF) will be

examined in this effort. Several measures of analysis performance are presented, including the standard assessment of an improved model fit to the assimilated observations. The impact of the cloud observations on key atmospheric parameters such as temperature, humidity, and cloud water content is also shown. A summary and conclusions are given in the final section.

2.Data assimilation algorithm

a. Basic equations

We employ the maximum likelihood ensemble filter (MLEF) data assimilation approach, developed at Colorado State University (Zupanski 2005, Zupanski and Zupanski 2006, Zupanski et al. 2008). The MLEF seeks a maximum likelihood solution of the posterior probability density function (PDF), which is equivalent to seeking a minimum of the following cost function (under the standard assumption of Gaussian PDFs for the observation and forecast errors):

$$J(x) = \frac{1}{2}(x - x^f)^T P_f^{-1}(x - x^f) + \frac{1}{2}[y - H(x)]^T R^{-1}[y - H(x)] \qquad (1)$$

The cost function (1) measures the differences between the model and the observations, where vector y of dimension N_{obs} (number of observations) is the observation vector, vector x of dimension N_S (model state dimension) is the model state vector, non-linear operator H is an observation operator, matrix R is the observation error covariance and matrix P_f is the forecast error covariance. The index 'f' refers to the forecast (used as a first guess). Superscript 'T' denotes transpose. The matrix P_f is defined in a subspace spanned by ensemble forecast perturbations as

$$P_f^{1/2} = (p_1^f \quad p_2^f \cdots p_{N_E}^f), \quad p_i^f = M(x^a + p_i^a) - M(x^a) \qquad (2)$$

where M denotes the non-linear forecast model, the superscript 'a' refers to the analysis and N_E is the number of ensembles. The vectors p_i^a and p_i^f represent columns

of the square roots of the analysis and forecast error covariances, respectively. The square root of the analysis error covariance is defined at the analysis solution x^a as

$$P_a^{1/2} = P_f^{1/2}[I_{N_E} + (Z(x^a))^T Z(x^a)]^{-1/2} \qquad (3)$$

where I_{N_E} is an $N_E \times N_E$ identity matrix and the matrix $Z(x^a)$ is the observation perturbation matrix at the analysis solution, defined by the following equation:

$$Z(x^a) = [z_1(x^a) \quad z_2(x^a) \quad \ldots \quad z_{N_E}(x^a)]$$
$$z_i(x^a) = R^{-1/2}[H(x^a + p_i^f) - H(x^a)] \qquad (4)$$

The inverse square root calculation in equation (3) is obtained via eigenvalue decomposition of the matrix $I_{N_E} + Z(x^a)^T Z(x^a)$. It is calculated as a symmetric square root, which is unique (e.g. Wang et al. 2004, Zupanski 2005, Wei et al. 2006).

We also calculate, as a diagnostic, the so-called information matrix C, of dimensions $N_E \times N_E$, defined in ensemble subspace as

$$C = Z(x^a)^T Z(x^a) \qquad (5)$$

which we use to calculate information measures, such as degrees of freedom for signal (DFS) defined as d (e.g. Shannon and Weaver 1949, Rodgers 2000, Zupanski et al. 2007)

$$d = \sum_{i=1}^{N_E} \frac{\lambda_i^2}{(1+\lambda_i^2)} \qquad (6)$$

where index 'i' denotes an ensemble member and λ_i^2 are eigenvalues of the information matrix C.

The χ^2 validation diagnostics (e.g., Menard et al. 2000), developed to validate the Kalman filter performance, can also be used in the context of ensemble-based data assimilation. This diagnostics evaluates the correctness of the innovation (observation minus forecast) covariance matrix R, and the MLEF-computed forecast error covariance

P_f. We adopt the definition used in Menard et al. (2000) - $\chi 2$ is defined in observation space, normalized by the number of observation, N_{obs}:

$$\chi^2 = \frac{1}{N_{obs}} \left[y_k - H(x_k) \right]^T (\mathsf{H}\mathsf{P}_\mathsf{f}\mathsf{H}^\mathsf{T} + \mathsf{R})^{-1} \left[y_k - H(x_k) \right]$$

In the MLEF algorithm, the above formula is rewritten as

$$\chi^2 = \frac{1}{N_{obs}} \left\{ \mathsf{R}^{-1/2} \left[y_k - H(x_k) \right] \right\}^T \mathsf{G}^{-1} \left\{ \mathsf{R}^{-1/2} \left[y_k - H(x_k) \right] \right\}$$

Where the matrix G^{-1} (e.g., its square root) is defined in appendix B in Zupanski (2005), y denotes observations, and x is the model forecast. Because of an iterative estimation of optimal analysis in MLEF, the forecast x denotes the forecast from the last minimization iteration, and the matrix C is calculated about the optimal state. For Gaussian distribution of innovations, and linear observation operator H, the conditional mean of χ^2 should be equal to 1. As in Menard et al. (2000), the conditional mean is substituted by a time mean. In this effort, the instant values of χ^2 is calculated at each assimilation cycle. Because of the use of a nonlinear model in calculation of P_f, and a statistically small sample (i.e., relatively few observations per cycle), one can expect only values of χ^2 close to 1 and not necessarily equal to 1.

b. Covariance localization

Covariance localization (e.g. Houtekamer and Mitchell 2001, Whitaker and Hamill 2002, Ott et al. 2004) is an effective way to account for the 'missing degrees of freedom' in ensemble-based data assimilation systems. By 'missing degrees of freedom' we mean that the number of degrees of freedom in the model state variable is much larger than the affordable ensemble size on a given computer. This often happens in applications to complex weather forecast model where the size of the model state variable could easily reach the order of 10^7-10^8, while the computationally feasible ensemble size can hardly be increased beyond the order of 10^2. In our experiments the size of the model

state vector x is $N_S \approx 3 \times 10^7$, thus it is several orders of magnitude larger than the ensemble sizes employed (32 members).

We adopted the covariance localization approach based on the so-called 'local domains', first proposed by Ott et al. (2004). In this approach, the entire model domain is partitioned into smaller local domains and the analysis solution is defined independently for each local domain. Due to the use of the globally defined forecast error covariance (P_f), overlapping local domains and/or some kind of smoothing, the assumption of 'independent local domains' is only partially enforced (e.g. Ott et al. 2004, Yang et al. 2009). The size of the local domains typically reflects the spatial scales of the processes being analyzed (e.g. extratropical or tropical cyclones, ocean currents, carbon transport), thus the assumption that the local domain are, to a degree, independent is considered appropriate. This covariance localization approach was successfully used, in slightly different variants, in many applications (e.g. Hunt et al. 2007, Miyoshi and Yamane 2007, Yang et al. 2009, Zupanski 2009a,b). We use the variant explained in Zupanski (2009a,b). Unlike the original Ott et al. (2004) approach, we use non-overlapping local domains, which ensure a well-posed minimization problem in each local domain and provide a straightforward definition of information measures, since each observation belongs to a single local domain and thus contributes to the information measures uniquely (Zupanski 2009a). A disadvantage of using non-overlapping local domain is in possible creations of discontinuities at the boundaries between local domains. To reduce these discontinuities, smoothing of the analysis weights is applied (e.g. Yang et al. 2009, Zupanski 2009a, b). The use of non-overlapping local domains, in conjunction with the smoothing, provided a satisfactory solution to the two contradictory requirements: to define a well-posed minimization problem over each local domain and to reduce discontinuous transitions from one local domain to another.

However, vertical error covariance localization is not used in this application of the MLEF, since it can also destroy the true vertical correlations and dynamical balances that exist in a hurricane (or any other well-formed cloud/precipitation system), and possible interfere with optimal use of microwave radiance observations due to the fact that there is no explicit vertical position.

It is worth mentioning that in the current implementation of the GSI-hybrid (Wang, 2010), the ensemble covariance is incorporated in the variational framework through the extended control variable method (Lorenc 2003; Buehner 2005; Wang et al. 2007, 2008), and the ensemble covariance localization is conducted in the model state variable space (i.e., model space localization); therefore, no assumption about the explicit position of the observation is required during this procedure of the covariance localization. For widely used EnKFs, explicit positions of the observations are needed to apply covariance localization (so-called observation space localization; Hamill et al. 2001). For satellite radiances, for which there is no explicit vertical position, such observation space localization is thus inappropriate.

c. Ensemble generation

How to generate an initial ensemble for regional application of EnDA system remains an open question because of the lack of accurate error statistics. The MLEF-HWRF may be initialized from an existing global or larger-scale ensemble. If a global ensemble forecast is not readily accessible, the most common alternative is to derive random perturbations from a static variational background error covariance of an existing 3D/4DVar system (e.g., Barker 2005; Meng and Zhang 2008), or to randomly sample the climatological uncertainties of the initial state (Aksoy et al. 2006). For our regional application of MLEF in TC vortex scale, random sampling may not be applicable because of its balance constraint and large scale.

To generate the first set of model states, the initial ensemble were generated by the time-shifted forecast technique as described in Zupanski et al. (2008). The initial 32-member ensemble is integrated for 6-h for evolve a flow-dependent forecast error covariance matrix before cloud-affected AMSU-A radiances are assimilated using the Maximum Likelihood Ensemble Filter. Compared with the commonly used random perturbation technique, the time-shifted ensemble perturbations reflect the model dynamics more realistically. Notice that the ensembles are initialized by time-shifted forecasts only in the first assimilation cycle. In all subsequent cycles the ensemble perturbations were defined by the standard ensemble-based covariance update.

The region of interest for this study lies within the vicinity of the hurricane inner and outer core, where large gradients in pressure, wind velocity, temperature, and moisture contribute to most of the forecast uncertainty. With this in mind, all calculations are performed in the region of HWRF (2011) inner domain that encompassed the eye, eyewall, and outer rainbands.

3. Inclusion of cloud-affected radiances

a. Cloudy radiance simulation.

A technique for the assimilation of AMSU-A radiance in the National Centers for Environmental Prediction's (NCEP's) global data assimilation is described in Zhang et al. (2013). Because the radiative transfer model used in the operational GSI does not yet allow for cloud/rain effects, it is crucial to properly identify cloud/rain-affected radiances using quality control (QC) and bias correction procedures. Both procedures require an accurate estimate of the total column cloud water.

We first define the fraction of ice and liquid cloud as:

Fraction of ice cloud (F): $F = (0°C - T)/20, \quad 0 \le F \le 1$

Liquid Cloud = Cloud Water × (1-F)

Ice Cloud = Cloud Water × F

We take advantage of a prognostic cloud scheme, which use explicitly determined condensate to compute cloud radiative properties. For liquid cloud, cloud optical depth, τ, single scattering albedo, ω, and asymmetry factor, g, are defined as:

$$\begin{cases} \tau_w = LWP(a_{0_w} + a_{1_w}/r_{e_w}) \\ 1-\omega_w = b_{0_w} + b_{1_w} r_{e_w} + b_{2_w} r_{e_w}^2 \\ g_w = c_{0_w} + c_{1_w} r_{e_w} + c_{2_w} r_{e_w}^2 \end{cases}$$

where LWP is cloud water path in unit of g/m^2, and r_e is the effective radius of water droplet in unit μm. The coefficients a, b, and c are prescribed using LUT. For ice clouds, τ, ω, and g are defined as:

$$\begin{cases} \tau_i = IWP(a_{0_i} + a_{1_i} / r_{e_i}) \\ 1-\omega_i = b_{0_i} + b_{1_i} r_{e_i} + b_{2_i} r_{e_i}^2 \\ g_i = c_{0_i} + c_{1_i} r_{e_i} + c_{2_i} r_{e_i}^2 \end{cases}$$

where IWP is cloud ice path, and coefficients a, b, and c are prescribed using LUT.

The parameterization of effective radius, r_e, of water droplet is similar to the method used by Kiehl et al. (1998) in the NCAR CCM3. We fix r_e to a value of 10μm over the oceans. Over the land, r_e is defined as:

$$r_e = 5.0 - 0.25T_c$$

Thus, the effective radius of cloud water droplets will reach to a minimum value of 5μm when temperature T_c is above $0°C$, and to a maximum value of 10μm when T_c becomes colder than -20°C.

For ice clouds, following Heymsfield and McFarquhar (1996), we have made the effective ice droplet radius to be an empirical function of ice water concentration (IWC) and environmental temperature as:

$$r_{e_i} = \begin{cases} (1250/9.917)IWC^{0.109} & T < -50°C \\ (1250/9.337)IWC^{0.080} & -50°C \le T < -40°C \\ (1250/9.208)IWC^{0.055} & -40°C \le T < -30°C \\ (1250/9.387)IWC^{0.031} & -30°C \le T \end{cases}$$

where IWC and IWP satisfy:

$$IWP_{\Delta Z} = \int_{\Delta Z} IWC dZ$$

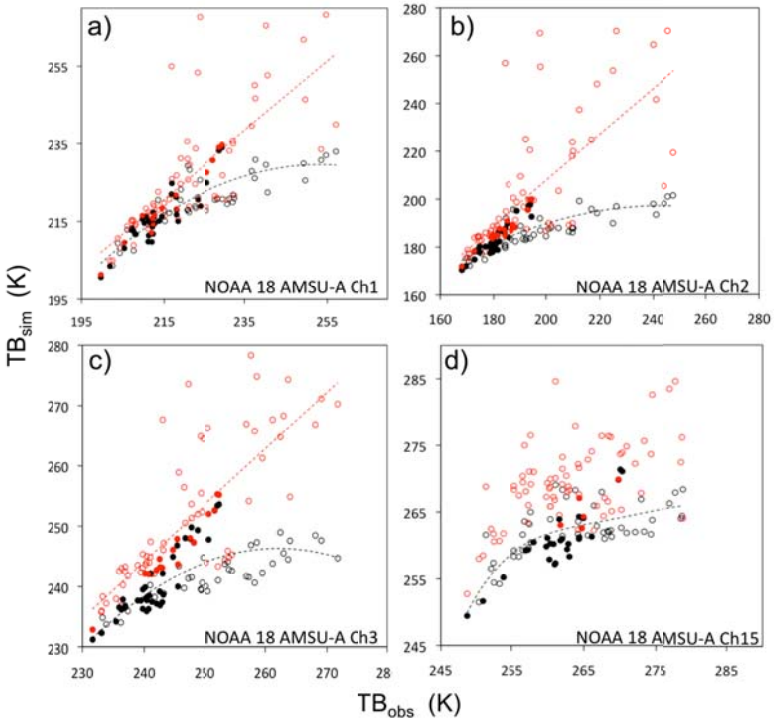

Figure 1. Comparison of observed TBs with the simulated from first guess with cloud ice/water profile calculation (red circles) and without cloud ice/ water profile calculation (black circles) for NOAA-18 AMSU-A (a) channel 1 (i.e., 23.8 GHz); (b) channel 2 (i.e., 31.4 GHz); (c) channel 3 (i.e., 50.3 GHz); (d) channel 15 (i.e., 89 GHz); valid at 1800 UTC 24 August 2010 in HWRF inner domain. The total number of observations is 75 following data thinning in 60 × 60 km box. Dashed lines denote the trend lines for each scenario. The corresponding red dots and black dots indicate those passed all quality control procedures and assimilated in the analysis.

Note that the cloud-affected AMSU-A radiances are assimilation through the GSI interface developed for MLEF-HWRF system, and thus can be independently assimilated using GSI system by other NOAA researchers. Before any experiments with assimilation of all-sky satellite radiances can begin, one has to quantify the impact of observation bias that is commonly found and corrected when assimilating clear-sky radiances. Although it may be straightforward to use cloud-cleared radiance bias correction, it is not clear whether this correction can be applicable for all-sky radiances, given that different atmospheric precursors may be responsible for bias when clouds and precipitation are present. In Fig.1 we show the impact of cloud-cleared radiance bias correction on (i) cloud-cleared radiance (CSR) and (ii) all-sky radiance (ASR) assimilation for AMSU-A channels 1-3 and 15. A perfect correction would imply all points on the straight line with a 45-degree angle.

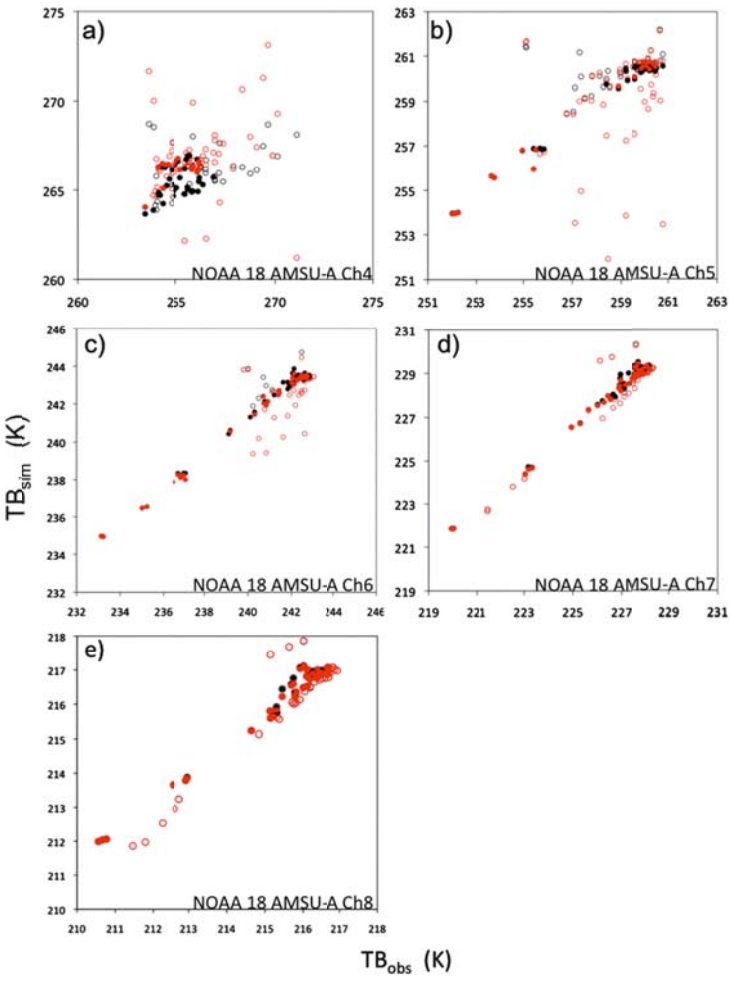

Figure 2. As in Fig.1, but for NOAA-18 AMSU-A (a) channel 4 (i.e.,52.8 GHz), (b) channel 5 (i.e., 53.5 GHz), (c) channel 6 (i.e., 54.4 GHz), (d) channel 7 (i.e., 54.9 GHz), and (e) channel 8 (i.e., 55.5 GHz) .

The all-sky approach has additional components required for allowing cloud-affected radiance assimilation, such as augmenting the analysis control variables to include clouds, as well as adding cloud guess profiles in the forward models.

b. Inclusion of CWM into control variables

The Joint Center for Satellite Data Assimilation (JCSDA) and the National Centers for Environmental Prediction (NCEP) have been working to assimilate cloud- affected microwave radiance data to improve the global analysis. It is planned to include AMSU-A radiance data affected by clouds over the ocean in the operational Global Data Assimilation System (GDAS) by 2013, and to move on to including cloud-affected microwave image data afterwards. The observation errors as a function of the mean

observed cloud amount and first-guess cloud amount have been estimated based on statistics of the first-guess departures for all-sky radiances following Geer and Bauer (2011). For now, *cloud water* (cw: liquid + ice) is being used as the control vector for all-sky radiance assimilation in addition to temperature, humidity, surface pressure, and surface winds, but *total moisture* (water vapor + cloud liquid + cloud ice + hydrometeors) as a control variable is currently being tested. The background error covariance matrix, in which error variances of cloud water are specified, is currently constructed by the NMC method.

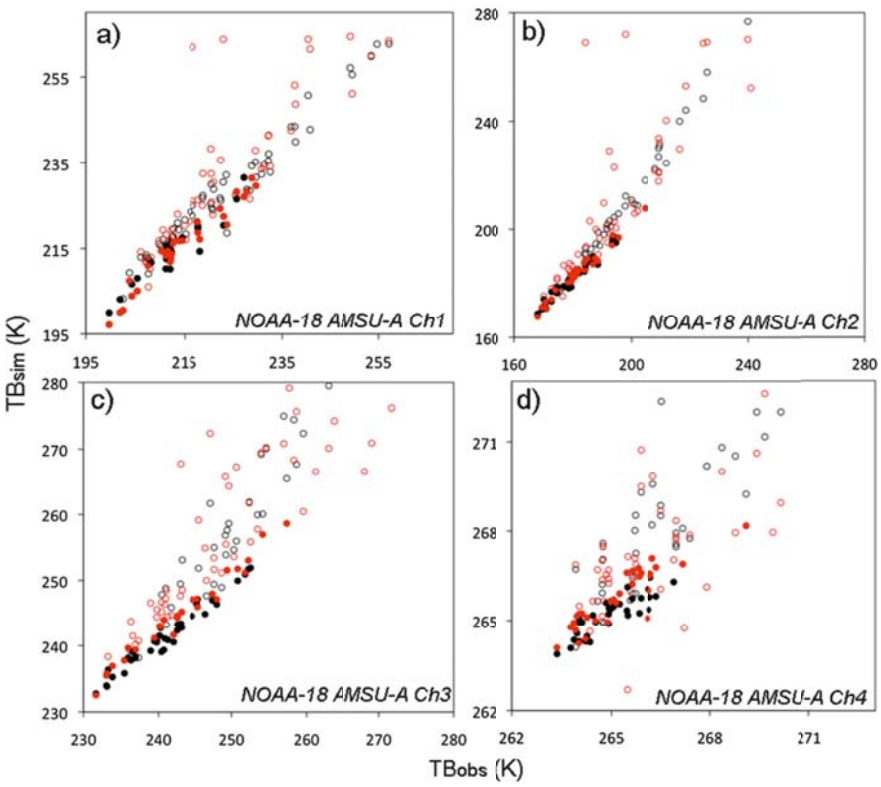

Figure.3. As in Fig.1, but for the comparison of observed TBs with the simulated TBs from channels (a) 1, (b) 2, (c) 3, and (d) 4, after being processed using the prescribed bias correction (red circles, ASR; black circles, CSR). The corresponding red and black dots indicate those data that passed all of the QC procedures and were assimilated into the analysis.

The extension of moisture-based control variables to cloud variables is currently also being investigated at ECMWF. The most likely option will be add cloud liquid water and cloud ice to the 'dry' control variables that are variance-normalized to produce Gaussian error covariance statistics as also employed for the moisture variable (Holm et

al. 2002). The Met office system already employs a total water control variable in both 4D-Var and 1D-Var systems.

c. Inclusion cloud profiles in the first guess fields

Over open ocean, a retrieved CLW from AMSU-A algorithms provided by Grody et al. (2001) are used. First, cloud liquid water (CLW) is derived using (o-g) brightness temperature of AMSU measurements at 23.8 and 31.3 GHz (channels 1 and 2).

$$CLW = \cos\theta\{D_0 + D_1 \ln[T_s - T_B(\nu_1)] + D_2 \ln[T_s - T_B(\nu_2)]\}$$

Where T_s is the surface temperature, and T_B, the brightness temperature at frequency at ν, can be obtained using the radiative transfer equation with absorption models for oxygen and water vapor (Rosenkranz, 1998). To ensure that $T_s > T_B(\nu)$ under all condition $T_s = 285K$ is chosen. The coefficients are given as

$$D_0 = 8.240 - [2.622 - 1.846\cos(\theta)]\cos(\theta)$$
$$D_1 = 0.754$$
$$D_2 = -2.265$$

The AMSU CLW compares well with ground-based sensors and other satellite measurements, although a bias exists between AMSU and TMI when the CLW exceeds 0.5 mm (Grody et al. 2001).

d. Bias correction and quality control

The radiance bias correction procedure may be one of the most important aspects of satellite radiance assimilation. In general, satellite channels may be prone to systematic errors due to instrument or radiative transfer problems, and these biases need to be corrected either before data enters into minimization procedure (statistical-based method, Harris and Kelly, 2001) or during minimization procedure (variational-based method, Dee and Uppala, 2009). Many research papers deal with the removal of these biases and most of them are based on global models and cloud-cleared radiances. Since direct assimilation of satellite radiances with the regional application is still in its infancy, our

strategy is to take advantage of the radiance bias correction scheme described by Derber and Wu (1998), in which predictor coefficients are already generated for cloud-cleared AMSU-A data using the NCEP Global Forecast System (GFS) model.

In NCEP operational GSI, a multi-step quality control (QC) procedure is applied to AMSU-A radiance data before data assimilation. First, AMSU-A radiances affected by cloud and precipitation are rejected. The cloud and precipitation screening procedure for microwave radiance observations in GSI is summarized as follows. The degree of non-precipitating cloud effect is determined by channel 4 related parameter, *factch4*, from an empirical relationship:

$$factch4 = clw^2 + \left[(tb_o^{ch4} - tb_c^{ch4}) \times 3\right]^2$$

Similarly, the degree of precipitating cloud affect is determined by channel 6 related parameter, *factch6*, from another empirical relationship:

$$factch6 = dsval^2 + \left[(tb_o^{ch6} - tb_c^{ch6}) \times 0.1\right]^2$$

where $(tb_o - tb_c)$ is the observed minus background brightness temperature after bias correction. The gradient of scattering index, *dsval* is determined depending on the surface type:

For sea surface:

$$dsval = \left\{\left[2.41 - 0.0098 \times (tb_o^{ch1} - cbias_{nadir}^{ch1})\right] \times (tb_o^{ch1} - tb_c^{tb1}) + 0.454 \times (tb_o^{ch2} - tb_c^{ch2}) - (tb_o^{ch15} - tb_c^{ch15})\right\} \times 0.1$$

For land surface:

$$dsval = 0.8$$

To account for possible degradation of measurement quality, if factch6≥1, the observation is considered affected by precipitation clouds and screened out. If factch4>0.5, the observation is considered affected by thick cloud and screened out. As

far as screening is concerned, observations in selected channels are rejected (see Table 1a).

Other QC steps include the following checks: (i) data over land are rejected due to the difficulties of modeling land surface emissivities and temperatures; (ii) all data located north of 40°N are discarded to avoid the degradation due to sea ice; (iii) inflating prescribed observation errors in different situations, such as topography effect, transmittance at the top of the model, and surface temperature and emissivity. The final QC step includes a general gross check ($i\,\mathrm{var}\,l$) that eliminates any observation for which the observation minus background innovation exceeds three times the standard deviation of observation error or the prescribed maximum error.

Table 1a. QC steps in subroutine qc_amsua (GSI3.0)

Category	*Quality Control steps*	*Action to observations*
qc1	Cloud affected profile (factch4 > 0.5)	Toss channel 1-5, 15
qc2	Inaccurate emissivity/surface temperature estimate over sea	Toss channel 1-5, 15
qc3	Cloud affected profile (Scattering index factch6 ≥ 1.0)	Toss channel 1-6, 15
qc4	Inflate observation error over high terrain (>2000m)	Inflate channel 6 observation error
qc5	Inflate observation error over high terrain (>4000m)	Inflate channel 7 observation error

Table 2a. The tossed and assimilated observation for each QC step at 1800 UTC 24 Aug 2010

	nobs	*qc1*	*qc2*	*qc3*	*qc4*	*qc5*	*ivarl*	*assim*
ASR	75	13	9	21	0	0	158	270

CSR	75	1	7	28	0	0	127	321

Taking the cloud-affected AMSU-A radiance assimilation configuration (ASR) as an example, we see there are 75 NOAA-18 AMSU-A profiles (or 75×9= 675 channel observations in channels 1-8, 15) in HWRF inner domain after data thinning, among which there are 158 channel observations that failed in the general gross check (*ivarl*). 13 profiles were tossed because of cloud affect based on factch4; 9 profiles were tossed because of inaccurate emissivity / surface temperature estimate over sea; 21 profiles were tossed because of cloud affect based on factch6; 0 profiles have inflated observation error because of high terrain (for both > 2000m and > 4000m); There are 270 channel observations passed all qc process and were used in analysis.

Obviously, there are two major factors leading to fewer observations assimilated in ASR configuration: *qc1* and *ivarl*. First, in this study we used the prescribed observation errors in GSI, which was designed for cloud-cleared radiance application and make more observations rejected in the gross check in the ASR configuration. On the other hand, the default QC1 step treats more observations as cloud-affected (factch4>0.5) in ASR. Ideally, some well-designed observation handling, errors, quality control and bias correction may have to be undertaken to address the cloudy radiance assimilation related issues (Geer and Bauer, 2011) and provide a weaker observational constraint on cloud analysis compared to the operational practice, which is beyond the scope of the present study. Nevertheless, the use of the hybrid data assimilation method and cloudy observation forward models may help produce more realistic analysis innovation and information content than the CSR configuration using the same data assimilation method.

4. Experimental design

As an initial attempt to reveal the potential of hybrid data assimilation for the direct assimilation of satellite radiances in the TC core area, this methodology was applied for one major hurricane case, Hurricane Danielle (2010). Danielle spanned the

period of 21–30 August 2010 and maintained hurricane strength beginning at 1800 UTC 23 August. In response to a new weakening in the subtropical ridge over the central Atlantic, a decrease in shear led to a gradual strengthening of the storm on 26 August. Danielle reached an intensity of 85 kt (1 kt = 0.5144ms^{-1}) at 1200 UTC 26 August with minimum central pressure of 973 hPa. Danielle eventually recurved southeast of Bermuda, never posing a threat to land. High-resolution visible satellite images from the Geostationary Operational Environmental Satellite-13 (GOES-13) (no shown) show that the clouds in a mature stage of Danielle are dominated by upper-level cirrus and cirrostratus, and there are rough tops of convective clouds penetrating through the smooth cirrostratus. At 1215 UTC 26 August, Danielle is an increasingly well-organized storm. The most striking feature around that time are the organized cloud bands spiraling anticyclonically outward, with a visible eye in the central core.

Since the aim of this study is to examine the impact of assimilating AMSU-A radiances in the TC core area, no other observations were assimilated. This approach provides an uncomplicated way to examine analysis increments of microphysical and thermodynamic variables induced by AMSU-A radiances. To evaluate the assimilation of cloud-affected AMSU-A radiances in the TC core area, two primary experiments are designed:

(i) the control experiment (CTL), which corresponds to the current operational practice of no data assimilation in TC core, and

(ii) sounding and window channel radiance assimilation (all channel radiances; ASR), which corresponds to a possible extension of the operational practice to assimilate both sounding and window channel radiances in the TC core with the proposed cloudy approach in previous section.

Two sensitivity experiments were also conducted to evaluate the impact of modeling clouds, by including cloud-guess profiles, and of omitting cloud-relevant channels in observations:

(iii) clear-sky radiance (CSR) assimilation, which is similar to ASR, but uses forward models in cloud-cleared conditions as the operational setting (i.e., no cloud-guess profiles are incorporated in forward models) and

(iv) sounding channels radiance assimilation (SND), which is similar to ASR, but excludes channels with weighting functions peaking below 700 hPa (i.e., channels 1–4 and 15). Since the lower-level peaking channels are more sensitive to cloud liquid water than other temperature sounding channels, the intention of this experiment is to identify if the hybrid data assimilation method, by varying the total-column condensate to fit channels 1–4, and 15, will improve the exclusive use of the temperature sounding channels. Observation errors used in analysis are taken from NCEP statistics.

Direct assimilation of satellite radiances using hybrid data assimilation with a regional model describing the TC core is fairly new and to the authors' knowledge has not yet been evaluated in any of the peer-reviewed literature. This configuration makes it more difficult to assess the benefits of satellite radiances because the assimilation cycle and model integration time are usually no longer than 3–4 days due to the small domain sizes. It is important to include a sufficient number of cycles so that (i) the accumulated statistics on analysis–forecast performance are meaningful and (ii) representative storm features are sampled. The MLEF-HWRF cycling system provides enough cases and addresses both of these issues. A total of nine cycles for each experiment were conducted, starting at 1200 UTC 24 August 2010, and ending at 1800 UTC 26 August 2010. The assimilation cycle interval is 6 h. The HWRF initial conditions at 1200 UTC 24 August 2010 are interpolated from the global analysis fields from GFS. The analysis is modified by the removal of the GFS vortex and the insertion of a bogus vortex based on theoretical considerations and HWRF climatology. This vortex is relocated and modified so that the initial storm position, structure, and intensity conform to the National Hurricane Center (NHC) storm message provided by the TC vitals. In the 2012 operational HWRF system, the storm is further modified using observations and the GSI system in the storm's environment. In this study, our initialization scheme skips the GSI analysis step in the operational HWRF vortex initialization. Note that the modified HWRF vortex initialization is only used at the start time of MLEF-HWRF cycling runs to restrict the

simulated storm. Once the MLEF-HWRF cycling runs begin, the analysis increments are influenced only by AMSU-A radiance assimilation within MLEF.

A 32-member ensemble is used in each experiment; thus, the ensemble size is several orders of magnitude smaller than the size of the control variable. To increase the number of degrees of freedom for the signal (DFS) in the assimilation, we employ error covariance localization (Yang et al. 2009) in the analysis, which includes the interpolation of observation weights in ensemble space. No vertical error covariance localization is applied in this study because of the possible interference with the optimal use of microwave radiances due to the fact that there is not explicit vertical position. Additionally, two minimization iterations of the nonlinear conjugate-gradient algorithm (Zupanski et al. 2008) were used in the data assimilation experiments.

5. Results

In this section, we first compare the simulated TBs with the measured observations under different forward model assumptions. Then, we investigate the structure of the MLEF flow-dependent error estimations and the implications for the cloudy satellite data assimilation. Finally, we show how different configurations can influence the accuracy of TC intensity and structure analyses, as well as short-range forecasts. We verify HWRF (2011) inner-domain forecasts through the 54-h forecasts period against various observations (e.g., NHC best-track data and satellite data), and examine information measures of AMSU-A radiances. Finally, we evaluate the sensitivity of the information content to channel selection and the forward model errors.

a. Validation of the radiance simulations

In Figs.1 and 2, the observed NOAA-18 AMSU-A radiances in the HWRF(2011) TC core area are compared to those simulated by the CRTM forward model with and without the inputs of cloud content profiles retrieved from the first guess. Since no bias correction is applied in this step, these comparisons allow for quantifying forward model biases based on different assumptions. Due to the low surface emissivity over the ocean

and the sensitivity to the surface temperature (or emissivity), TBs fields simulated from cloud-cleared CRTM at channels 1-3 and 15 (open black dots in Fig.1) appear to have a cold bias compared to the measured TBs. However, the inclusion of modeled clouds, which have higher emissivity, results in a significant "warming" for warmer atmospheres. Obviously, the overall agreement between the measured and simulated radiances with cloudy radiance simulation is more reasonable for cloudy and rainy conditions. Since channels 4-8 are responsive to average air temperature and atmospheric constituents at increasingly higher altitudes through the troposphere, the simulated TBs are less sensitive to the inclusion of modeling clouds (Fig.4) compared with those of window channels. It is also evident that some of the simulated cloudy TBs in channels 5 and 6 have cold biases, although these observations are not ingested into the analysis. The biases are presumably due to the effects of the scattering of large ice/liquid cloud particles that survived from the default quality control procedures.

We further compare the TBs statistics after using cloud-cleared bias correction (BC) and quality control (QC) procedures. In Fig.3, we demonstrate that the prescribed BC scheme has a competitive degree of performance in the cloudy radiance simulation. Furthermore, the resulting distributions after BC and QC are Gaussian, with the maximum number of observations at or near zero, which further confirms that the agreement between the observed and simulated TBs are very good. Simulations without cloud profile inputs generally have low biases, and these errors are only marginally increased in cloudy simulations. Also notice that due to the use of operational QC procedures, the AMSU-A observations are removed if thick clouds or precipitation is detected, which is based on the retrieved cloud liquid water and a retrieved scattering index. Therefore, our assimilation results are valid only for nonprecipitating thin clouds, which are also evident in Fig.4. In Figs.4e-h, the areas of significant cloud absorption are highlighted by positive departures, since cloud-cleared radiative transfer simulation for these lower-level peaking channels underestimates the atmospheric contribution added by relatively warm clouds over the radiometrically cold surface. However, a colder temperature departure is evident in Figs.4a-d. It is worth mentioning that the main differences between the two simulations occur when thick clouds or precipitating conditions prevail, even though only nonscattering/nonprecipitating clouds are

assimilated in this study. Nevertheless, it is interesting to examine if the inputs from the model cloud profiles lead to a better simulation of the TC core area structure.

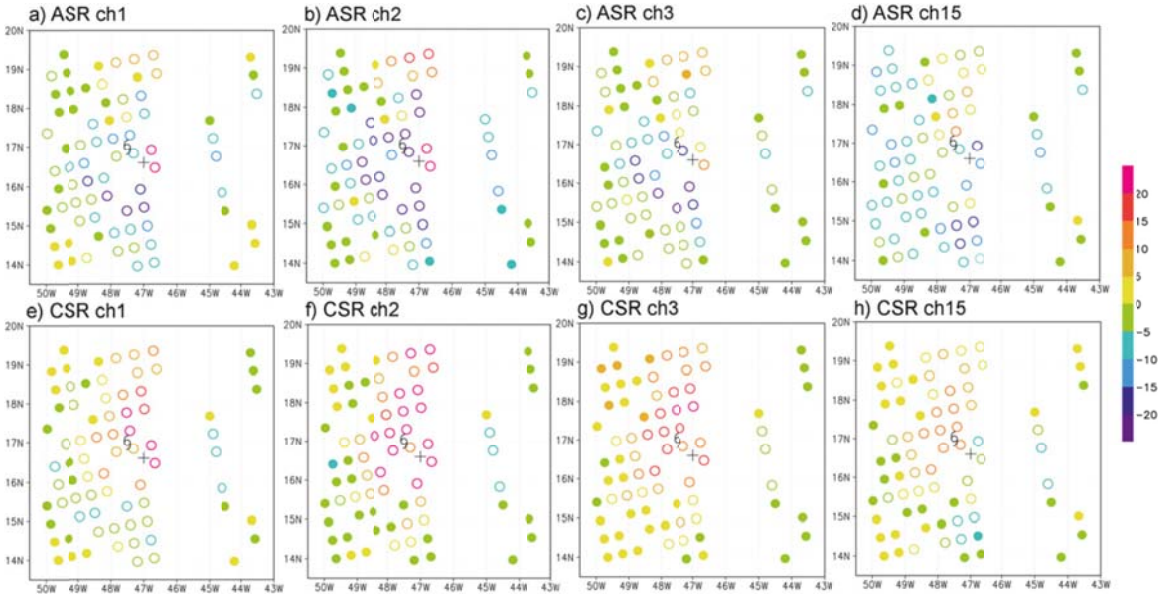

Figure.4. The NOAA-18 AMSU-A TBs observations minus the cloudy CRTM-simulated background TBs (K; ASR experiment) before bias correction and data thinning in a 60 km × 60 km box, from channels (a) 1, (b) 2, (c) 3, and (d) 15 at 1800 UTC 24 Aug 2010. Observation locations at which the observed radiances do and do not pass the QC process are indicated by solid dots and open circles, respectively. (e)-(h) as in (a)-(d),but for the CSR experiment. The plus sign denotes the simulated storm, and the observed storm is also indicated. (This is the same for the rest of the figures when applicable.)

b. Forecast error dynamics

The formulation of the forecast error covariance and the choice of control variables represent two important elements in a multivariate optimization problem. The structure of the forecast error covariance is fundamental since it defines a mathematical subspace where analysis correction is performed. The square root of the diagonal of this matrix defines a standard deviation that can be used as a measure of uncertainty. It is therefore important to investigate the structure and uncertainty produced by a flow-dependent forecast error covariance in the TC core area.

An example is shown in Fig.5 depicting ensemble errors in Danielle's core region valid at 0600 UTC 25 August 2010. The ensemble error quantifies sample standard deviations for a given variable, and represents the posterior uncertainty provided by the MLEF. It is evident that the forecast uncertainty is significantly larger in the TC core region, not only in hydrometeor mass (i.e., column-integrated CWM), but also in other

kinematic and thermodynamic fields. For example, the forecast uncertainty of CWM responds to the high-CWM region. In the vertical cross section, the errors in temperature perturbation (Fig.6a) are tilted with the radius of maximum wind (RMW), shown in Fig.6b. The significant forecast uncertainty in low-level wind fields (Fig.6b), which is related to variations of moist convection in the TC core region, is especially large near the ocean interface and close to the RMW. Larger values indicate the potential for larger corrections from observations in this area during the data assimilation procedure. These results also indicate that the forecast errors evolve with time, propagate with the flow, and can be determined by the underlying storm dynamics.

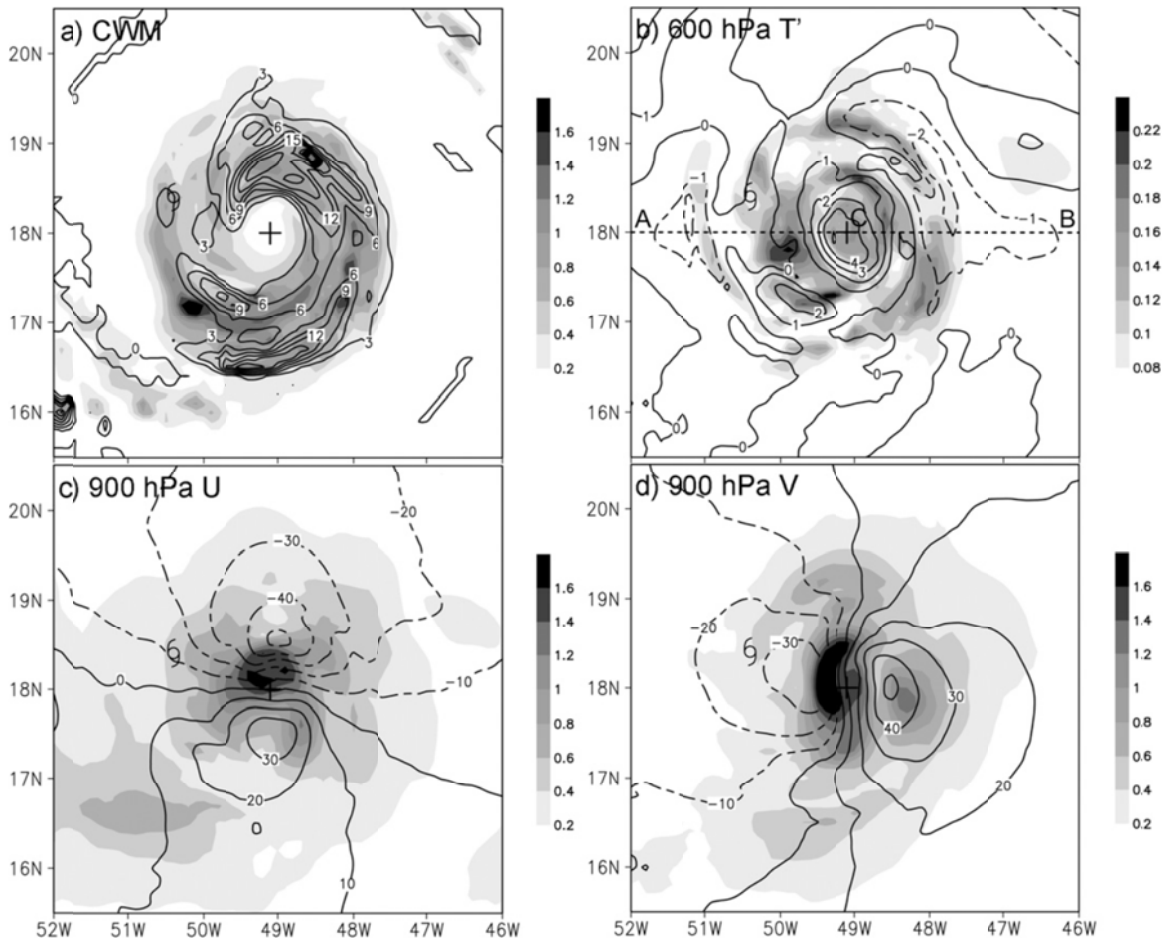

Figure.5. The horizontal distribution of the optimal analysis state (solid/dashed lines) and the standard deviation (shading) of (a) the vertical cumulated CWM (kgm^{-2}), (b) the temperature perturbation (K) at 600 hPa, (c) u (ms^{-1}) at 900 hPa, (d) v (ms^{-1}) at 900 hPa. All figures are valid for the analysis at cycle 3 (i.e., 0600 UTC 25 Aug 2010).

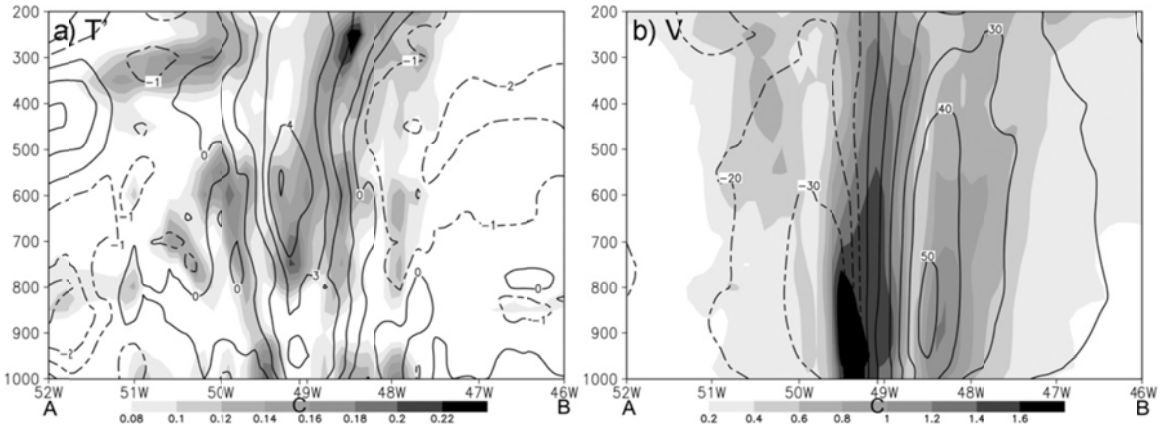

Figure.6. As in Fig.5, but for the vertical cross section of (a) *T* perturbation (K) and (b) *v* (ms^{-1}), along the latitude of the storm center at 18°N.

Through auto- and cross covariance, the information from a single observation can spread to nearby locations and to other variables as well. To illustrate how error covariance responds to an isolated unit perturbation generated by a single observation, we consider a single pseudo-observation of temperature at model level 23 (about 400 hPa) (Fig. 7). This would correspond to an observation of AMSU-channel 6 radiance sensitive to temperature at location C (20.42°N, 52.88°W). Figures 7a and 7b show the horizontal responses of the temperature and CWM fields, respectively, at the same level. The auto covariance of the temperature indicates a positive response at the observation location, as is expected. The same is true for the CWM response to temperature perturbation (Fig.7b), indicating that warming implies more clouds. In addition, the horizontal response between the temperature perturbation and wind indicates a divergence, which is also evident as vortex weakening. Figure 7c shows the vertical response of CWM to temperature perturbation. It is evident that there is strong vertical correlation between forecast errors in temperature and hydrometeor content, implying an impact on the analysis throughout the vertical column. In other words, if an AMSU-A channel 6 observation senses warming temperatures at one location, this information will be extended to generate an analysis response in the hydrometeor content in the nearby column and, therefore, influences the cloud analysis throughout the troposphere.

c. Verification of assimilation results against observations

Assimilation statistics in Table 2 shows that the observations minus the analysis (OMA) RMS errors over the whole data assimilation period are indeed lower than the observations minus the background (OMB) ones for almost all active channels in the ASR experiment, indicating a positive impact of analysis. Similar results can be found in other radiance assimilation experiments. The forecast tracks of Danielle obtained from the MLEF-HWRF 6-h cycling system are also compared with the NHC best-track data (Fig. 8). The forecast tracks generally agree with the observed track, in which the observed storm turned northwestward later on 25 August.

To further demonstrate the system's capability in reproducing rapid deepening of Danielle, the time series of the minimum mean sea level pressure (MSLP) 6-h forecasts are compared with the NHC best-track data (Fig.9). Since the 6-h forecast initialized with the analysis obtained by the radiance assimilation at a previous analysis time was used as a background field, the impact of AMSU-A radiance observations propagates gradually into the atmospheric levels, where no observations are available (e.g., the MSLP fields). The HWRF vortex initialization tends to overestimate the MSLP of Danielle at the start time of the data assimilation (i.e., 1200 UTC 24 August 2010) in this study. Although the CTL produced a deeper storm than was observed during the 54-h data assimilation period, the MSLP forecast trend is comparable to the observations. For both the ASR and CSR experiments, during the first 24-h period, the simulated MSLP decreased at a rate slower than the CTL experiment, and more similar to the observed. During the last 30 h, the storms in CSR and SND keep weakening, while the deepening trend of the ASR storm became closer to the observed after cycle 5, and eventually matched the best-track storm MSLP after cycle 8. The difference is apparently due to the unique information extraction capability of the ASR approach.

Now let us shift our attention to the verification of the storm vortex-scale features, using the combined sum of the hydrometeor variables (i.e., CWM). The simulated column-integrated CWM indicates how well the model predicts the precipitation field and the rainfall rate. Figure 10a displays a *MetOp-A* AMSU-A-retrieved precipitation rate map valid at bout 1h later than those in Figs.10b-e. It is interesting to note that the precipitation pattern in Fig.10a generally agrees with the visible satellite imagery around

this time (not shown). In Fig. 10a, the eyewall with about 50-km radius is shown as a semicircular ring of heavy convective precipitation. The rainbands closest to the eyewall, about 200 km from the TC center, are dominated by stratiform precipitation, with broad uniform coverage and very little convective precipitation. In the outer region, organized rainbands spiraled outward in the northern quadrant of the storm. All of these features are asymmetric, with primary rainbands located on the downshear side. In the Fig.10c, the ASR-simulated storm size, the cloud condensate distribution, and the area of intense convection compare favorably to the distribution of observed precipitation. In particular, the ASR reproduced organized rainbands that spiraled outward along the north edge of the eyewall with an intense convective center embedded in the rainbands in the northeastern quadrant. The active convection center corresponds to the maximum rainfall core of greater than 20 mm h^{-1} in Fig.10a. Also well reproduced are weaker centers embedded within the stratiform precipitation on the inner side of the maximum rainfall center. Although the ASR experiment reproduces most of the significant cloud features, a detailed comparison shows a few deficiencies with the simulation. For example, the observed precipitation rate map displays an eyewall with a radius of about 50 km, which is not reproduced in any experiment. Additionally, the ASR experiment also underestimates the radius of the outer rainbands in the northeastern quadrant. These deficiencies are likely related to the relatively coarse horizontal resolution (i.e., 9 km) of the HWRF (2011) inner domain, which cannot resolve intense convective cells at a scale of a few kilometers within the eyewall. It is expected that the 2012 triple-nested HWRF system with 3-km horizontal resolution near the hurricane core can further address these shortcoming (Tallapragada et al. 2012).

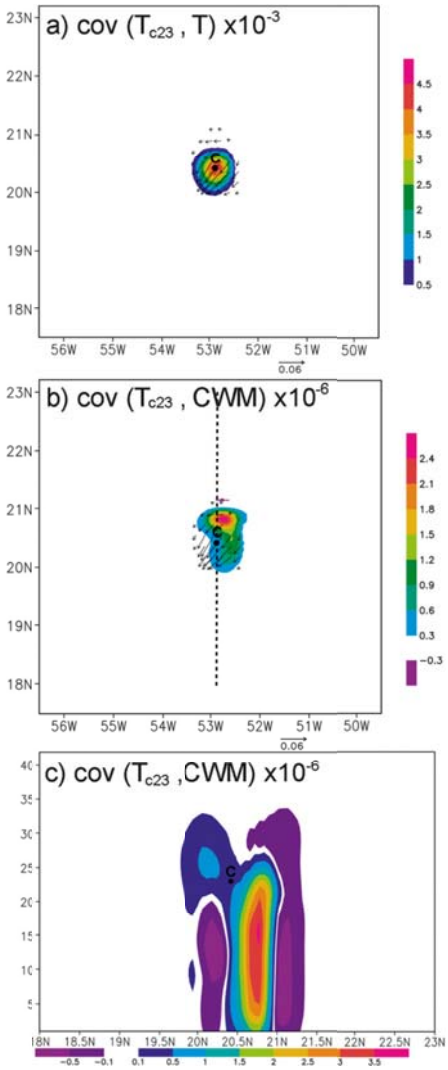

Figure.7. Background error covariance, illustrated by plotting a portion of the error covariance corresponding to a single observation perturbation on temperature at model level Z=23 (about 400 hPa), 20.42°N, 52.88°W, valid at 1800 UTC 25 Aug 2010. (a) Horizontal error autocovariance of T_{c23} and T at Z=23. (b) Horizontal error cross covariance of T_{c23} and CWM at Z=23. (c) Vertical error cross covariance of T_{c23} and CWM at 52.88°W. The horizontal error cross covariance of Tc23 and wind at Z=23 is also indicated in (a) and (b) by the vectors.

TABLE 2. Data usage statistics related to the ASR experiment. These include the number of observations ingested after data thinning, and passing all QC processes for all channels and cycles, as well as RMS errors of AMSU-A observation departures from the background (OMB) and from the analysis (OMA). If the RMS error of OMA is lower than that of OMB, it is in boldface. Calculations were carried out in the HWRF inner domain over nine cycles from 1800 UTC 24 Aug to 1800 UTC 26 Aug 2010.

	Channel 1	Channel 2	Channel 3	Channel 4	Channel 5	Channel 6	Channel 7	Channel 8	Channel 15
					Cycle 1				
No. of obs	27	26	26	30	47	51	36	12	15
OMB	2.292	2.663	2.113	0.766	0.367	0.277	0.425	0.445	2.839
OMA	**2.078**	**2.451**	**2.112**	**0.633**	**0.343**	0.281	**0.41**	**0.389**	**2.346**
					Cycle 3				
No. of obs	20	20	22	22	41	48	51	10	18
OMB	2.16	2.028	1.442	0.643	0.338	0.24	0.354	0.418	2.538
OMA	**2.103**	**1.63**	**1.388**	**0.641**	**0.287**	**0.204**	**0.349**	**0.406**	**2.267**
					Cycle 5				
No. of obs	24	25	32	33	52	53	82	42	20
OMB	2.35	1.76	2.15	0.488	0.299	0.277	0.324	0.361	2.396
OMA	**2.258**	1.948	2.262	**0.455**	**0.292**	**0.228**	**0.322**	0.366	**2.263**
					Cycle 6				
No. of obs*	17	16	19	19	49	58		15	17
OMB	1.994	2.897	1.780	0.567	0.326	0.183		0.410	2.373
OMA	**1.543**	**2.894**	**1.641**	**0.555**	0.330	0.20		0.418	**2.076**
					Cycle 7				
No. of obs	27	30	32	32	62	65	75	29	27
OMB	2.726	2.099	1.439	0.39	0.282	0.182	0.294	0.341	1.619
OMA	**2.651**	**2**	1.475	**0.369**	**0.278**	**0.171**	**0.289**	**0.329**	1.849
					Cycle 9				
No. of obs	14	14	18	18	34	40	52	32	15
OMB	2.722	2.713	1.686	0.430	0.364	0.228	0.294	0.380	1.945
OMA	**2.615**	**2.400**	1.738	**0.386**	**0.347**	**0.227**	**0.250**	0.424	**1.613**

* AMSU-A observations from *MetOp-A* assimilated in this cycle; otherwise those from *NOAA-18* are assimilated.

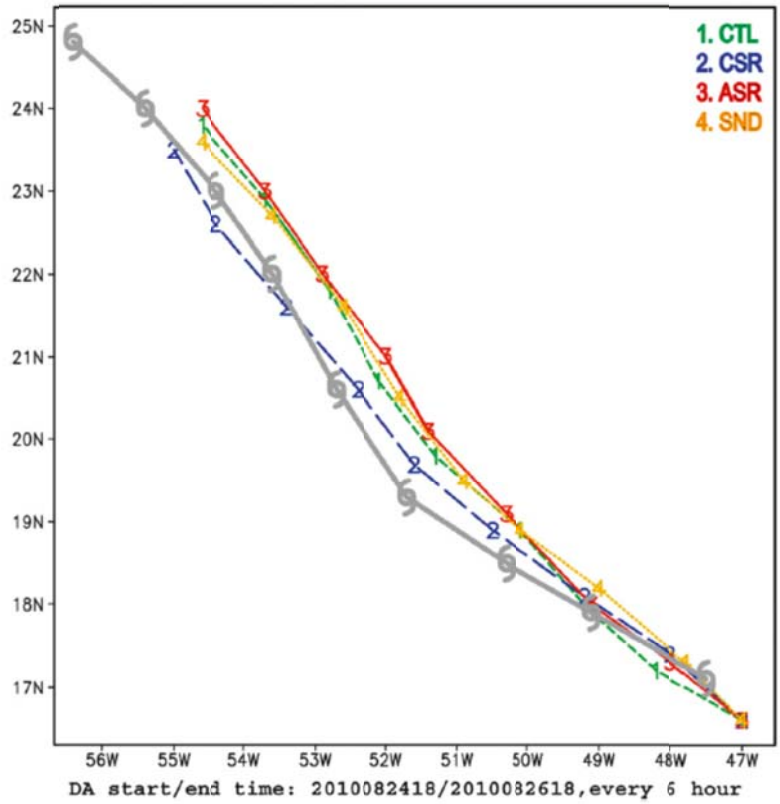

Figure.8. Tracks of Hurricane Danielle from the 6-h best-track data (denoted by the TC symbol) from the NHC and the CTL/CSR/ASR/SND experiment forecasts are given between 1800 UTC 24 Aug and 1800 UTC 26 Aug 2010 every 6 h.

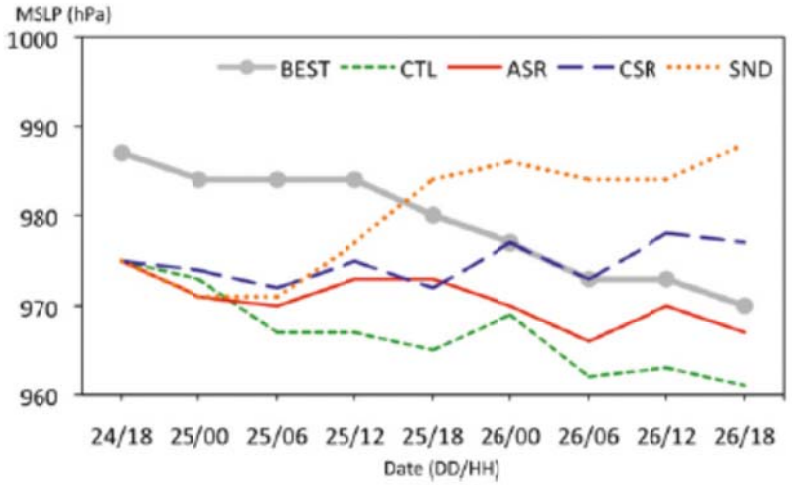

Figure.9. Time series of the MSLP (hPa) and NHC best-track data (thick gray line), and MLEF-HWRF 6-h forecasts between 1800 UTC 24 Aug and 1800 UTC 26 Aug 2010 every 6 h (i.e., cycles 1-9)

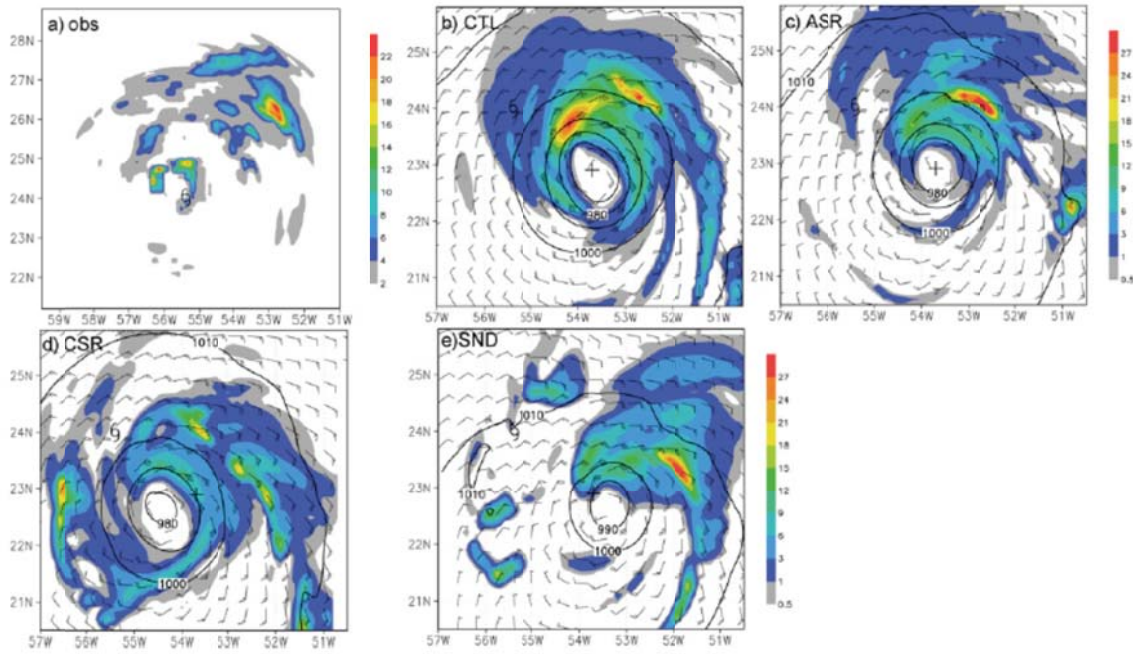

Figure.10. (a) AMSU-retrieved precipitation rate map from MetOp-A at 1311 UTC 26 Aug 2010 (mm h^{-1}). Distribution of the 6-h CWM (colored; kg m^{-2}) forecasts start from cycle 7 analyses of the (b) CTL, (c) ASR, (d) CSR, and (e) SND experiments, superposed with MSLP and 10-m above wind barbs, valid at 1200 UTC 26 Aug 2010.

By contrast, the CTL-simulated cloud condensate distribution differs markedly from the observations and the ASR experiment. The CTL simulation exhibits two convective centers embedded within the "distant rainbands" (Houze 2010) in the northern quadrant. In addition to the significant departures in storm deepening after the first 24 h of integration in the CSR case, compared with the CTL and ASR experiments (Fig.10), it

is also obvious at cycle 7 that similar departures are seen in the CSR cloud and MSLP distributions (Fig.10d). It is worth noting that the SND experiment, to a certain extent, reproduced the horizontal distribution of the column condensate in the northeast quadrant, such as the intense convective center and the stratiform region on its inner side. However, the deficiency of the SND experiment in surface wind and MSLP intensity indicates that the reproduction to the realistic cloud structure is attributed to assimilating lower-peaking channels of cloudy satellite radiances. Overall, the ASR approach produced a storm that is most similar to the observed storm in many aspects, compared to the other experiments. In particular, the simulated asymmetry in the convective structure has important implications with respect to the improvement of quantitative precipitation forecasts (QPFs), wave height forecasts, and severe wind warnings if the storm is about to make landfall.

Information content in ensemble subspace (Zupanski et al.2007) was developed using information theoretical concepts elucidated by Shannon and Weaver (1949) and through the application of their technique to atmospheric science by Rodgers (2000). In MLEF, the amount of information contained in the observations is quantified by comparing the effective signal to noise ratios. This is accomplished practically through the analysis of the information matrix in the ensemble subspace, of dimensions $N_{ens} \times N_{ens}$, which holds the key to understanding and quantifying the differences between various forward models and the observations data. This study uses the same definition and formula as Zupanski et al.(2007). The overall features of the information content analysis (i.e., the spatial distribution of DFS) have been gathered together in Fig. 11, which shows the information content that is added through the combination of different forward models and channel selection (i.e., ASR/CSR/SND experiments). In Fig.11, we plotted the DFS obtained in experiments with 10×10 subdomains (e.g., pixels). The DFSs are calculated for each of the 100 local blocks and quantify the impact of the observations in each local block. The flow-dependent DFS indicates the utility of AMSU-A radiances in the HWRF (2011) inner domain. In the first cycles, the correlated forecast differences imply a reduction of DFS in the information content or the forecast error covariance due to the utility of the time-shifted ensemble perturbations at the beginning of the data assimilation. However, the number of DFSs quickly increases given that there is

sufficient error growth in ensemble prediction with HWRF. This increasing is particularly evident near the center of the TC core area for the ASR experiment and to a lesser extent for the SND experiment, suggesting that the observations are influencing the region of the TC that is often poorly observed in the current HWRF due to the clear-sky assumption. It is also indicated that the ASR configuration provides the most integrated information over all of the cases shown. These results further demonstrated that an entropy-based definition of information content provides a powerful metric for evaluating the utility of a set of observations and simulated satellite radiances in a hybrid data assimilation method.

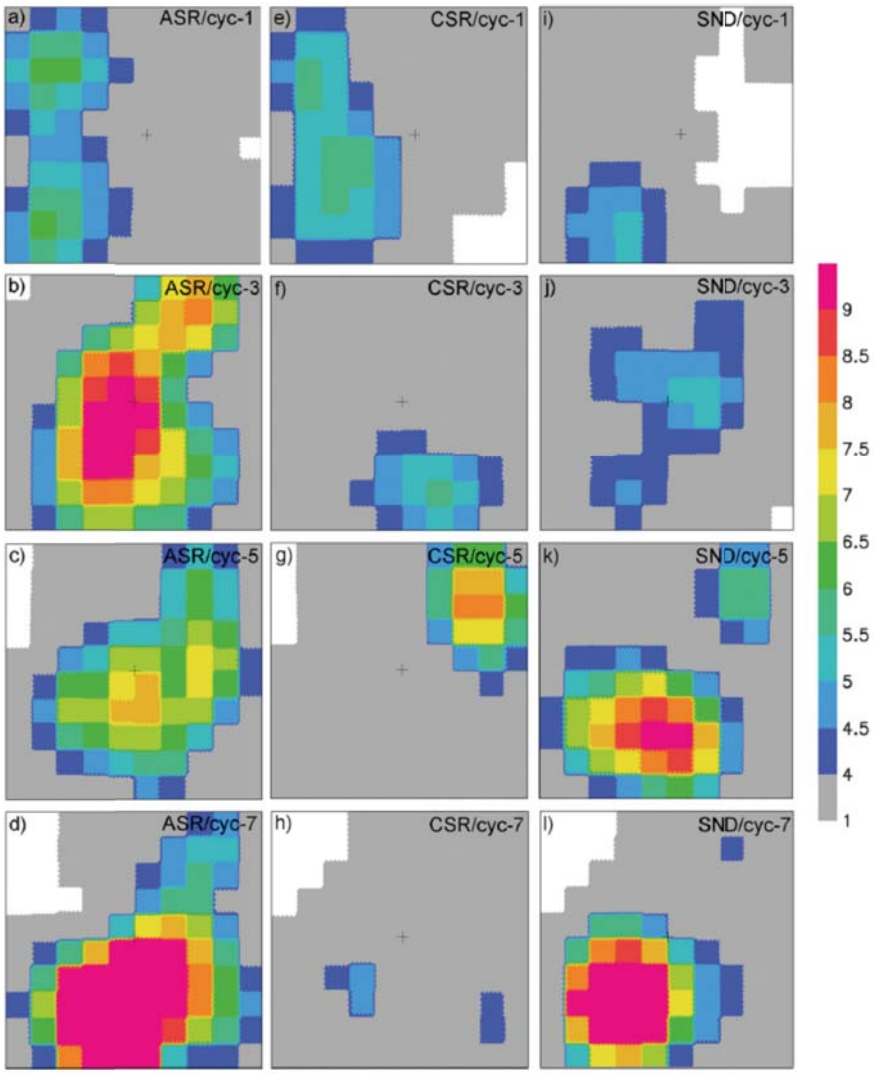

Figure 11. Information content results of the assimilated observations (DFSs) calculated in the distinct data assimilation configurations are shown for cycles 1, 3, 5, and 7. The DFS are nondimensional quantities. All

figures are plotted in an HWRF inner domain (i.e., with a scale of 6°×6°) centered at the simulated storm center. Larger values indicate a greater influence of the observation in the data assimilation.

6. Summary

Currently, no inner-core satellite radiances are directly assimilated in NCEP operational NWP models, including both GFS and HWRF systems. However, these observations of clouds and precipitation may hold the key to improving vortex initialization and ultimately TC intensity prediction. In this study, a prototype hybrid variational–ensemble data assimilation system (HVEDAS) is used to identify the impact of the direct assimilation of satellite radiances in the TC core area. The assimilation experiments are conducted using MLEF with NOAA operational codes that include the atmospheric component of the HWRF (2011) model and the forward components of the GSI analysis system and the CRTM. Specifically, the AMSU-A radiances from NOAA-18 and MetOp-A are assimilated into Hurricane Danielle (2010) with the maximum likelihood ensemble filter (MLEF), which better addresses the nonlinearity of the observation operators than more common EnKF methodologies by employing an iterative minimization of a cost function. The new approach has additional components required for allowing cloud-affected radiance assimilation, such as augmenting the analysis control variables to include clouds and adding cloud-guess profiles in the forward models. The CRTM forward model biases are first calculated in the HWRF inner domain based on both cloud-cleared and cloudy radiance simulation assumptions, which are required for the assimilation of cloudy satellite radiances. The results suggest that the cloudy AMSU-A radiance simulation outperforms the cloud-cleared simulation across all NOAA-18 AMSU-A channels and that the operational data processing procedures are correctly adjusting for any remaining systematic differences on a TC core area basis. It is also shown that through the prescribed ‘‘cloud cleared’’ bias correction and quality control procedures, the simulated and observed TB fields show good agreement for all NOAA-18 AMSU-A channels.

The ensemble uncertainty analysis is found to be highly anisotropic and time dependent. The horizontal autocorrelation of a pseudo-AMSU-A channel 6 observation produces an isotopic, Gaussian-like shape as a function of distance. In turn, complex microphysical processes in the TC core area imply that hydrometeor mass variables will be cross correlated with temperature and produce different horizontal and vertical structure functions. The flow-dependent structures of error cross covariance between temperature and hydrometeor variables provide a means for observation information on temperature affected by nonscattering clouds to influence hydrometeor fields as well. Furthermore, our results demonstrate the necessity of gaining a better understanding of the error growth mechanism and the related storm dynamics for the TC core region.

The performance of the HVEDAS and the value of cloudy radiance assimilation added to the analyses and forecasts of Danielle (2010) core area are assessed by a comparison with observations. In particular, we performed cycling data assimilation experiments at 6-h intervals for a length of 54 h to examine the performance when reproducing the observed storm track, intensity/MSLP, and vortex-scale structure. In general, the impact on the storm track was marginal. However, a particularly encouraging result was the improvement in the storm intensity forecasts over the operational control experiment. The proposed ASR approach tends to outperform the operational and cloud-cleared radiance experiments. With the cloud affected AMSU-A radiance assimilated, the system reasonably captures the rapid deepening stage of Hurricane Danielle, and reproduces a measurable positive impact on the TC intensity prediction, as well as on the hydrometeor structures through multivariate correlations of microwave radiances and thermodynamical fields, and model integration. The results also show that the entropy-based information content of the data, as measured by the degrees of freedom for signal (DFS), was significantly increased, implying a more efficient use of the observations in the ASR experiment.

Although a case study, this study provides insights and potential solutions for future TC prediction, especially for the TC structure including intensity forecasts. Our results suggest that a hybrid data assimilation algorithm could provide an objective, observation-based way of incorporating a dynamically consistent vortex with reasonable

asymmetries into the initial conditions of the current triple-nested 2012 operational HWRF system operating at 3-km horizontal resolution near the hurricane core. This study paves the way for the assimilation of other data types in the cores of TCs. Data from new microwave sounders and scatterometers, as well as aircraft-based data, if used within this framework, offer even further opportunities to improve the TC vortex initialization of operational forecast models.

Publications and Conferences/Workshops (2013, April – 2014, April)

Zhang, M., M. Zupanski, M-J. Kim and J. A. Knaff (2013): Assimilating AMSU-A Radiance in the TC Core Area with NOAA Operational HWRF (2011) and a Hybrid Data Assimilation System: Danielle (2010). *Mon. Weather Rev.*, *141* (11) 3889-3907

Zhang, M., M. Zupanski, J.A. Knaff: Direct Assimilation of All-sky SEVIRI IR10.8 Radiances in TC Core Area Using an Ensemble-based Data Assimilation Method. *WMO Sixth Symposium on Data Assimilation*, 7 Oct, 2013, College Park, MD, United States

Reference

Aksoy, A., F. Zhang, and J. W. Nielsen-Gammon, 2006:Ensemble-based simultaneous state and parameter estimation with MM5. *Geophys. Res. Lett.,* **33**, L12801, doi:10.1029/2006GL026186.

Barker, D. M., 2005: Southern high-latitude ensemble data assimilation in the Antarctic Mesoscale Prediction System. *Mon. Wea. Rev*., **133**, 3431-3449.

Buehner, M., 2005: Ensemble-derived stationary and flow-dependent background-error covariances: Evaluation in a quasi-operational NWP setting. *Quart. J. Roy. Meteor. Soc.*, **131**, 1013-1043.

Dee, D. P., 1995: On-line estimation of error covariance parameters for atmospheric data assimilation. *Mon. Wea. Rev.,* **123**, 1128-1145.

Dee, D. P., and S. Uppala, 2009: Variational bias correction of satellite radiance data in the ERA-Interim reanalysis. *Q. J. R. Meteorol. Soc.,* **135**, 1830-1841.

Derber, J. C., and W.-S Wu, 1998: The use of TOVS cloud-cleared radiances in the NCEP SSI analysis system. *Mon. Wea. Rev.*, **126**, 2287-2299.

Errico, R. M., P. Bauer, J-F. Mahfouf, 2007: Issues regarding the assimilation of cloud and precipitation data. *J. Atmos. Sci*., **64**, 3785-3798.

Geer, A. J. and P. Bauer, 2011: Observation errors in all-sky data assimilation. *Q. J. R. Meteorol. Soc.*, **137**, 2024-2037.

Grody, N., J. Zhao, R. Ferraro, F. Weng, and R. Boers, 2001: Determination of precipitable water and cloud liquid water over oceans from the NOAA 15 advanced microwave sounding unit. *J. Geophys. Res.*, **106**, 2493-2953.

Hamill, T. M., J. S. Whitaker, and C. Snyder, 2001: Distance-dependent filtering of background error covariance estimates in an ensemble Kalman filter. *Mon. Wea. Rev.*, **129**, 2776-2790.

Harris B. and G. Kelly, 2001: A satellite radiance bias correction scheme for data assimilation. *Q. J. R. Meteorol. Soc.*, **127**, 1453-1468.

Heymsfield, A. J., and G. M. McFarquhar, 1996: High albedos of cirrus in the tropical Pacific warm pool. *J. Atmos. Sci.*, **53**, 2424-2451.

Holm, E., E. Andersson, A. Beljaars, P. Lopez, J.-F. Mahfouf, A. Simmons, and J.-N. Thepaut, 2002: Assimilation and modeling of the hydrological cycle: ECMWF's status and plans. Tech. Rep. 383, ECMWF, 55pp.

Houtekamer, P. L. and H. L. Mitchell, 2001: A sequential ensemble Kalman filter for atmospheric data assimilation. *Mon. Wea. Rev.*, **129**, 123-137.

Hunt, B. R., E. J. Kostelich, and I. Szunyogh, 2007: Efficient data assimilation for spatiotemporal chaos: a local ensemble transform Kalman filter. *Physica D*, **230**,112-126.

Kiehl, J. T., J. J. Hack, G. B. Bonan, B. A. Boville, D. L. Willamson, and P. J. Rasch, 1998: The National Center for Atmospheric Research community climate model: CCM3. *J. Clim.,* **11**, 1131-1149.

Lorenc, A. C., 2003: The potential of the ensemble Kalman filter for NWP-A comparison with 4D-VAR. *Q. J. R. Meteorol. Soc.,* **129**, 3183-3203.

Menard, R., S. E. Cohn, L.-P Chang, and P. M. Lyster, 2000: Assimilation of stratospheric chemical tracer observations using a Kalman filer. Part I: Formulation. *Mon. Wea. Rev.,* **128**, 2654-2671.

Meng, Z., and F. Zhang, 2008: Tests of an ensemble Kalman filter for mesoscale and regional-scale data assimilation. Part III: Comparison with 3DVAR in a real-data case study. *Mon. Wea. Rev*., **136**, 522-540.

Miyoshi, T., and S. Yamane, 2007: Local ensemble transform Kalman filtering with an AGCM at T159/L60 resolution. *Mon. Wea. Rev.*, **135**, 3841-3861.

Moreau, E., P. Lopez, P. Bauer, A. M. Tompkins, M. Janisková, and co-authors, 2004: Variational retrieval of temperature and humidity profiles using rain rates versus microwave brightness temperatures. *Q. J. R. Meteorol. Soc*. **130**, 827-852.

Ott, E., B. R. Hunt, I. Szunyogh, A. V. Zimin, E. J. Kostelich, M. Corazza, E. Kalnay, D. J. Patil, and J. A. Yorke, 2004: A local ensemble Kalman filter for atmospheric data assimilation. *Tellus*, **56A**, 273-277.

Rodgers, C. D., 2000: *Inverse Methods for Atmospheric Sounding: Theory and Practice*, 238 pp, Singapore: World Scientific.

Rosenkranz, P., 1998: Water vapor continuum absorption: a comparison of measurements and models. *Radio Sci*, **33**, 919-928.

Shannon, C.E. and W. Weaver, 1949: *The Mathematical theory of Communication*, 144 pp, Urbana: University of Illinois Press.

Vukićević, T., T. Greenwald, M. Zupanski, D. Zupanski, T. Vonder Haar, and co-authors, 2004: Mesoscale cloud state estimation from visible and infrared satellite radiances. *Mon. Wea. Rev.,* **132**, 3066-3077.

Wang, X., C. H. Bishop and S. J. Julier, 2004: Which is better, an ensemble of positive/negative pairs or a centered spherical simplex ensemble? *Mon. Wea. Rev.*, **132**, 1590-1605.

Wang, X., C. Snyder, and T. M. Hamill, 2007: On the theoretical equivalence of differently proposed ensemble/3D-Var hybrid analysis schemes. *Mon. Wea. Rev*., **135**, 222-227.

Wang, X., D. Barker, C. Snyder, and T. M. Hamill, 2008: A hybrid ETKF-3DVAR data assimilation scheme for the WRF model. Part I: Observing system simulation experiment. *Mon. Wea. Rev*., **136**, 5116-5131.

Wang, X., 2010: Incorporating Ensemble Covariance in the Gridpoint Statistical Interpolation Variational Minimization: A Mathematical Framework. *Mon. Wea. Rev*., **138**, 2990-2995.

Wei, M., Z. Toth, R. Wobus, Y. Zhu, C. H. Bishop and X. Wang, 2006: Ensemble transform Kalman filter-based ensemble perturbations in an operational global prediction system at NCEP. *Tellus*, **58A**, 28-44.

Whitaker, J. S. and T. M., Hamill, 2002: Ensemble data assimilation without perturbed observations. *Mon. Wea. Rev.*, **130**, 1913-1924.

Yang, S.-C., E. Kalnay, B. Hunt and N. E. Bowler, 2009: Weight interpolation for efficient data assimilation with the local ensemble transform Kalman filter. *Q. J. R. Meteorol. Soc.*, **135**, 251-262.

Zupanski, D., 2009a: Information measures in ensemble data assimilation. *Data Assimilation for Atmospheric, Oceanic, and Hydrologic Applications*, S. -K. Park and L. Xu (Eds.), pp. 85-95, Berlin: Springer-Verlag.

Zupanski, D., A. Y. Hou, S. Q. Zhang, M. Zupanski, C. D. Kummerow, and S. H. Cheng, 2007: Application of information theory in ensemble data assimilation. *Q. J. R. Meteorol. Soc.*, **133**, 1533-1545.

Zupanski, D., and M. Zupanski, 2006: Model error estimation employing ensemble data assimilation approach. *Mon. Wea. Rev.*, **134**, 1337-1354.

Zupanski, M., 2005: Maximum Likelihood ensemble filter: theoretical aspects. *Mon. Wea. Rev.*, **133**, 1710-1726.

Zupanski, M., 2009b: Theoretical and practical issues of ensemble data assimilation in whether and climate. *Data Assimilation for Atmospheric, Oceanic, and Hydrologic Applications*, S. –K. Park and L. Xu (Eds.), pp. 67-84 (Berlin: Springer-Verlag).

Zupanski, M., I. M. Navon, and D. Zupanski, 2008: The maximum likelihood ensemble filter as a non-differentiable minimization algorithm. *Quart. J. Roy. Meteor. Soc.*, **134**, 1039-1050.